

Signal-to-noise estimates of time-reverse images

Ben Witten* and Brad Artman, Spectraseis AG

SUMMARY

Locating subsurface sources from passive seismic recordings is difficult when attempted with data that has no observable arrivals or a low signal-to-noise ratio. Using time-reversal techniques recorded energy can be focused at its source depth. However, when a focus cannot be matched to a particular event, it can be difficult to distinguish true focusing from artifacts. Artificial focusing could arise from numerous causes, including surface waves, local noise sources, acquisition geometry and velocity model effects. We present a method to more reliably locate subsurface sources that reduces the ambiguity of the results. Time-reverse imaging techniques are implemented on both the recorded data and a noise model. In the data domain, the noise model only approximates the energy of local noise sources. After imaging, however, the result also captures the effects of acquisition geometry and the velocity model. The noise image is then used to correct the data image to produce an estimate of the signal-to-noise ratio. Synthetic data examples show the versatility of this technique to varying amounts of noise and to challenging velocity models. A field data example shows how this technique can be used to locate the source of low-frequency energy collocated with an oil reservoir.

INTRODUCTION

To better understand physical processes in the subsurface, accurately identifying the location of an event, often from passive measurements, is important for many applications. Tools to locate subsurface events are regularly applied to reservoir and CO₂ sequestration monitoring (Maxwell et al., 2004), induced micro-fracture localization (Maxwell and Ubancic, 2001), and hydrocarbon exploration (Steiner et al., 2008) which focus energy at the source. These measurements, however, often have low signal-to-noise ratios that have no identifiable events in the data. With no evident arrivals, separating the true source focusing and focusing due other effects is not trivial. Artificial focusing can arise due to factors such as, noise sources in the data, including surface waves, sampling artifacts, or velocity model effects. We introduce noise images as an estimate of these artifacts in the image domain. The noise image is then used to correct the data image to produce an estimate of the signal-to-noise ratio.

IMAGING AND PROPAGATION

Our method begins with time-reverse modeling (TRM) which was developed to locate sources from acoustic measurements (Fink, 1999). It is the process of injecting a time-reversed seismic wave field at the recording locations and propagating it through a velocity model. We then apply an imaging condition to produce a single image in physical space. The chain of

operations of propagating a time-reversed wave field through a model and applying an imaging condition is the process we call time-reverse imaging (TRI). For the examples presented here, elastic propagation is used. We define two imaging conditions here. The first, I_a , is the zero lag of the autocorrelation of the wave field amplitude,

$$I_a(\mathbf{x}) = \sum_t |\mathbf{u}(\mathbf{x}, t)| |\mathbf{u}(\mathbf{x}, t)|, \quad (1)$$

where $\mathbf{u}(\mathbf{x}, t)$ is the wave field in 1-, 2-, or 3- spatial dimensions, and propagation time, t . Alternatively, the wave field can be decomposed into its constituent P- and S-wave components and a cross-correlation imaging condition can be constructed (Artman et al., 2009). It is defined as

$$I_{ps}(\mathbf{x}) = \sum_t P(\mathbf{x}, t) S(\mathbf{x}, t). \quad (2)$$

Because the wave field is sampled at discrete locations, artificial energy is created when injecting the data, which corrupts the image (Xuan and Sava, 2009). Figure 1 shows a time snapshot of a subsampled horizontal plane wave of vertical particle motion through a homogeneous medium. The wave-front has healed sufficiently to approximate the full wave field, clearly seen at a depth of approximately 2200 m. However, numerous artifacts, manifested as superposed circular wave fronts, exist behind the coherent wave-front. These artifacts are mainly high-ray-parameter energy, traveling at high angles. This includes all of the S-wave energy, which is purely artificial here. Field data will also contain surface wave energy that has similar characteristics to these artifacts. In either case, artifacts or surface waves, this energy is problematic when locating body wave sources at depth. Therefore, a means to attenuate it is necessary.

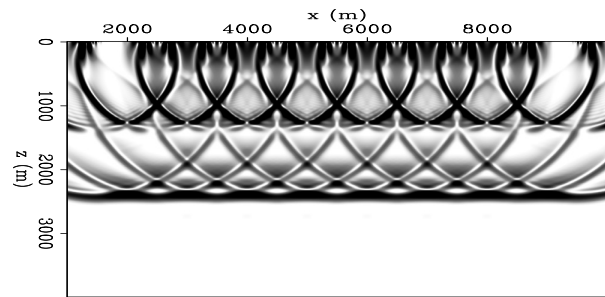


Figure 1: Time snapshot of the absolute wave field amplitude from a sub-sampled plane wave propagating through a homogeneous medium.

In a $v(z)$ earth model, energy will bend according to Snell's Law. Because the artifacts and surface waves exist mainly at high ray parameters, their effects are mitigated by propagation. Energy at high angles becomes evanescent and are effectively trapped in the near surface. Figure 2 shows the result of the

Image domain SNR

I_{ps} imaging condition after propagating the subsampled plane wave through a homogeneous (left) and a 0.8 km/s/km gradient (right) velocity model. The solid lines are traces extracted from a recording/injection location and the dashed lines are taken from between recording locations. If the full plane wave was sampled and imaged, there would be zeros everywhere because there is no real S-wave energy. Due to the limitations of the sparse recording, S-wave energy is introduced and is a sampling artifact. In the homogeneous medium case, these artifacts propagate throughout the model and cause non-zero artifacts at all depths. However, in the gradient velocity case, S-waves, which have no vertically propagating energy, continually overturn and reflect off the surface causing extremely high values in the near surface. This energy, however, does not affect the image at depth. Since the earth generally has increasing velocity with depth, propagating field data to depth with the TRI algorithm ensures that most of the energy imaged at depth is not artifacts or surface waves. Therefore propagation through a $v(z)$ medium, increasing with depth, is a surface-wave filter.

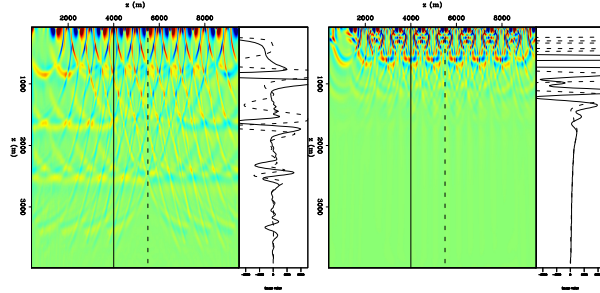


Figure 2: Left: I_{ps} image of a sub-sampled horizontal plane wave with vertical particle motion through a homogeneous medium. Right: I_{ps} image of the sub-sampled plane wave through a gradient velocity. The solid lines are a traces extracted from recording locations and the dashed line is taken between recording locations.

SIGNAL TO NOISE IMAGES

Now that it has been shown that, at depth, TRI results attenuate sampling artifacts and surface waves, we must ensure that no bias due to noise and the velocity model exist. We call this bias the system response and define it as the cumulative effects of the acquisition geometry, velocity model, and noise in the image domain. This includes the near-surface effects seen previously. To accurately interpret the signal contribution, we must estimate and remove the system response from the TRI result.

We start by defining a noise model as random traces that are scaled to the amplitude of the field data after bandpassing to the frequency band of interest. This guarantees that the noise traces have equal energy to the recorded traces but without any correlated phase information between the traces. The advantage of this type of noise model is that it is based directly on the data. No information about the acquisition environment is

necessary. The disadvantage is that it can only account for uncorrelated noise sources across the array. Other noise models can be generated, with the most accurate noise model providing the best results.

Once created, the estimated noise data is imaged with the TRI algorithm in the same fashion as the field data, creating the system response. The system response will take the role of an estimated noise model to incorporate into the signal-to-noise estimate presented by Melton and Bailey (1957). While those discussions develop the signal-to-noise quantity in the data domain, we introduce the analogous formalism to the image domain.

We start by assuming the recorded data, d , is a combination of signal and noise: $d = s + n$. The image created from this data is the apparent signal image, I , which will contain contributions from both the signal and the system response. The apparent signal for the recorded data for an autocorrelation imaging condition, such as equation 1, is defined as:

$$I = \sum_t (s_t + n_t)^2 = \sum_t s_t^2 + 2s_t n_t + n_t^2, \quad (3)$$

where t is the time-axis over which we sum for correlation. For conciseness we will drop this subscript. For cross-correlation imaging conditions, such as equation 2, a similar equation can be constructed. The estimated noise image, \tilde{N} , is defined as:

$$\tilde{N} = \sum \tilde{n}^2, \quad (4)$$

where \tilde{n} is the estimated noise data. Next we divide equation 3, by the estimated noise image, \tilde{N} . Before division, \tilde{N} is smoothed for stability. Rearranging terms and substituting the definitions of I and \tilde{N} , we obtain an estimated signal to noise ratio at each model location:

$$\tilde{I} = \frac{I}{\tilde{N}} = \frac{\sum s^2}{\sum \tilde{n}^2} + 2 \frac{\sum sn}{\sum \tilde{n}^2} + \frac{\sum n^2}{\sum \tilde{n}^2}. \quad (5)$$

The division of two images from data sets that we have, I and \tilde{N} , results in the right hand side of equation 5. If the noise has been estimated correctly, then $n \approx \tilde{n}$ and $\frac{\sum n^2}{\sum \tilde{n}^2} \approx 1$. Any departure from this value of 1 provides an indication of how well the noise has been estimated away from the source location.

SYNTHETIC EXAMPLES

To demonstrate the advantages of the estimated signal to noise images, we will create synthetic data sets. A single 15 second time trace is constructed from 50 randomly distributed vertical single forces of random amplitude with a central frequency of 3.5 Hz. This trace is then injected into the model at one location (3500,6000) and elastically propagated through a 0.8 km/s/km gradient velocity model with a constant V_p/V_s ratio and density. The resulting wave field is recording at the surface at 250 meter intervals. Noise is added to the data and we apply the estimated signal to noise imaging procedure.

Figure 3 shows the wave field amplitude auto-correlation imaging results from these tests (equation 1). The black dot indicates the true source position. Noise has been added to the data

Image domain SNR

such that it has signal-to-noise ratios of (from left to right) ∞ , 0.5, and 0.25. The signal-to-noise ratio of the data will be abbreviated as DSNR to distinguish it from the image domain signal-to-noise ratio, ISNR. The top row shows the apparent signal image, I_a , generated from equation 3, and the bottom row shows the estimated signal-to-noise images, \tilde{I}_a , from equation 5. The images on the left are the best possible given the acquisition geometry because $\text{DSNR} = \infty$. Despite this, numerous artifacts still exist in the apparent signal image (top) in the near surface due to not fully sampling the wave field. By dividing by the noise model, the system response has been removed and the artifacts are greatly reduced in the estimated signal-to-noise image (bottom). For $\text{DSNR} = 0.5$ (middle column), the focusing at the source location in the apparent signal image is poorly separated from the noise above. The artifacts in the near surface are stronger than the focus at the source location. The estimated signal-to-noise image has, again, removed the artifacts and enhanced the source focusing with respect to the background. The apparent signal image generated from $\text{DSNR} = 0.25$ (left), has only a slight indication of focusing at the source location. It is much weaker than the energy in the near surface. The estimated signal-to-noise image is still clearly defined and easily interpretable with the strongest focus around the source location.

FIELD DATA EXAMPLE

A low-frequency passive seismic survey was conducted over and around an oil discovery in the Egyptian desert. One-hundred ten stations continuously recorded over approximately 60 hours. Figure 4 shows acquisition geometry of the survey. The discovery well location is located at the intersection of AA' and BB'. The data was selected to be the quietest 3 minutes of the recorded data between 1 and 6 Hz. We will focus on lines AA' and BB' shown in Figure 4.

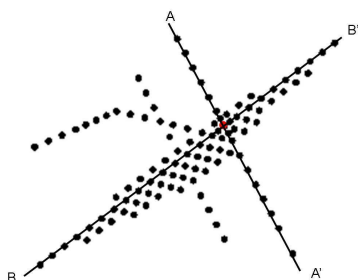


Figure 4: Acquisition geometry of the field survey.

Since all the stations were recording synchronously, 3D TRI was implemented. This allows for all three components to be utilized in the propagation and allows the energy to coalesce appropriately in (x,y,z) -space. Figure 5 is a depth slice from the 3D cube near the approximate reservoir depth. A strong central area of high ISNR values is clearly evident around the structural high. No other areas show consistent values above 1, $\text{ISNR} \approx 0$.

Figure 6 shows extracted lines along AA' and BB' from the 3D

TRI volume overlayed on the reflection seismic images. By integrating the TRI results with the other geologic and geophysical information, such as the reflection seismic volume, a better understanding of the subsurface may be achieved. While the reflection seismic volume provides structural information, the TRI can add another piece of information related to the fluid properties (Riahi et al., 2009; Goloshubin et al., 2006).

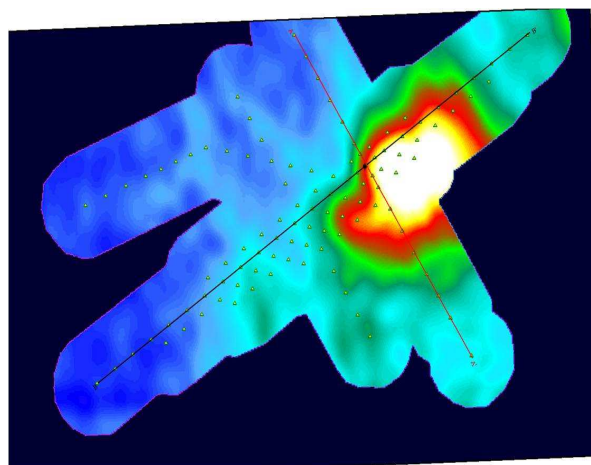


Figure 5: Depth slice from the 3D \tilde{I}_a TRI cube at the reservoir interval.

CONCLUSIONS

We present a method for locating subsurface sources from passive recordings based on time-reversal that corrects for the contributions of acquisition geometry, surface waves, noise, and velocity model effects. It can be used for any source type, but is particularly useful for data with a low signal-to-noise ratio or with no observable arrivals. Our method reduces the ambiguity in results by utilizing a noise model to simultaneously correct for the effects of under-sampling the wave field, localized surface noise sources, and effects due to the velocity model. This creates an estimate of the signal-to-noise ratio at every point in the physical, (x,y,z) , space. The method is flexible to any acquisition geometry and can be applied to complex velocity fields. When used as a complementary tool along with the structural information of reflection seismology, it can be used to evaluate prospective areas. In the field data example presented, we have shown that the TRI image shows a strong source focusing that is spatially collocated with the structural high and known hydrocarbon.

ACKNOWLEDGEMENTS

We would like to thank Shell Egypt for allowing us to publish the field data results.

Image domain SNR

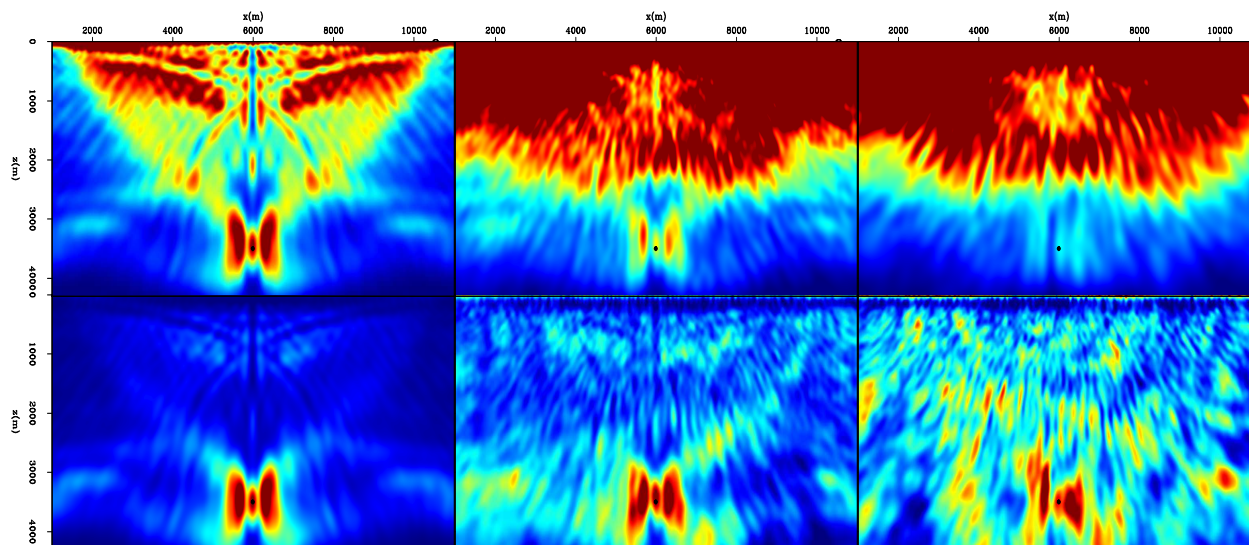


Figure 3: Top: apparent signal images, I_a , generated from DSNR of (from left to right) ∞ , 0.5, and 0.25. Bottom: estimated signal to noise images, \tilde{I}_a generated from the same data as above.

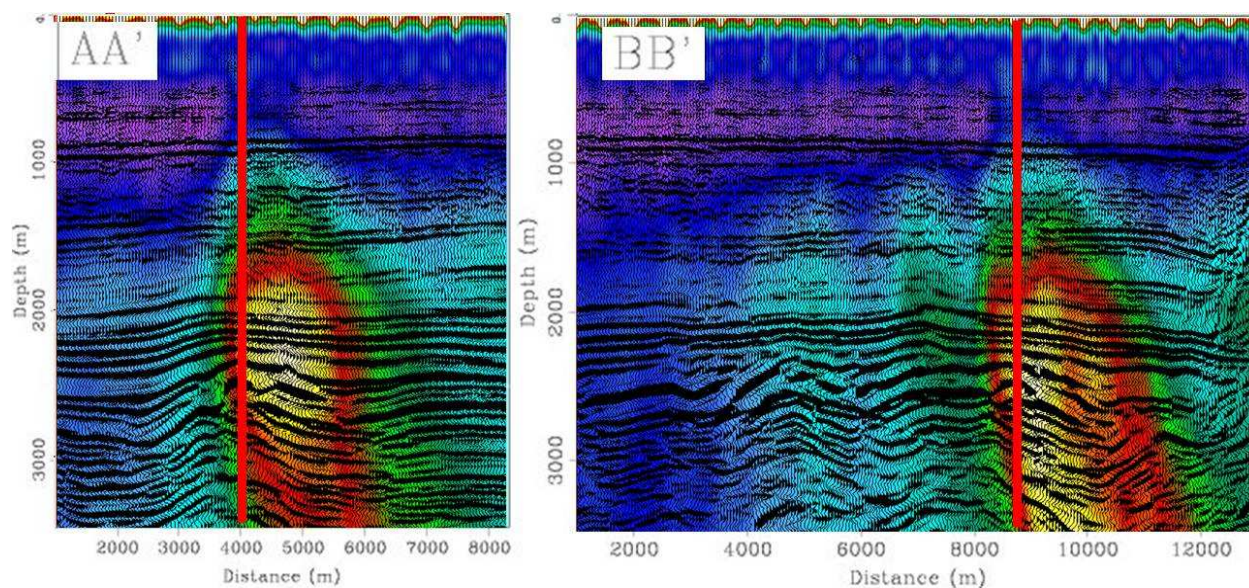


Figure 6: 3D \tilde{I}_a TRI images of lines AA' and BB' overlaid on a reflection seismic section. The red line indicates the lateral location intersection of the lines at the discovery well.

EDITED REFERENCES

Note: This reference list is a copy-edited version of the reference list submitted by the author. Reference lists for the 2010 SEG Technical Program Expanded Abstracts have been copy edited so that references provided with the online metadata for each paper will achieve a high degree of linking to cited sources that appear on the Web.

REFERENCES

- Artman, B., I. Podladtchikov, and A. Goertz, 2009, Elastic time-reverse modeling imaging conditions : SEG Technical Program Expanded Abstracts, **28**, 1207–1211.
- Fink, M., 1999, Time-reversed acoustics: Scientific American, November, 67–73.
- Goloshubin, G., C. V. Schuyver, V. Korneev, D. Silin, and V. Vingalov, 2006, Reservoir imaging using low frequencies of seismic reflections : The Leading Edge, **25**, no. 5, 527–531, [doi:10.1190/1.2202652](https://doi.org/10.1190/1.2202652).
- Maxwell, S., and T. Ubancic, 2001, The role of passive micro- seismic monitoring in the instrumented oil field : The Leading Edge, **20**, no. 6, 636–639, [doi:10.1190/1.1439012](https://doi.org/10.1190/1.1439012).
- Maxwell, S., D. White, and H. Fabriol, 2004, Passive seismic imaging of co2 sequestration at weyburn: SET Extended abstracts, SET, 568.
- Melton, B. S., and L. F. Bailey, 1957, Multiple signal correlators: Geophysics, **22**, 565–588, [doi:10.1190/1.1438390](https://doi.org/10.1190/1.1438390).
- Steiner, B., E. H. Saenger, and S. M. Schmalholz, 2008, Time reverse modeling of low-frequency microtremors: Application to hydrocarbon reservoir localization: Geophysical Research Letters, **35**, no. 3, L03307, [doi:10.1029/2007GL032097](https://doi.org/10.1029/2007GL032097).
- Xuan, R., and P. C. Sava, 2009, Probabilistic micro-earthquake location for reservoir monitoring and characterization: Geophysics, submitted for publication.